RSC Advances

This article can be cited before page numbers have been issued, to do this please use: H. L. Pan, Q. Q. Liu, Y. H. Zhang and H. T. wu, *RSC Adv.*, 2016, DOI: 10.1039/C6RA20197K.

ROYAL SOCIETY OF CHEMISTRY

www.rsc.org/advances

View Article Online
DOI: 10.1039/C6RA20197K

Crystal structure and microwave dielectric characteristics of Co-substituted $Zn_{1-x}Co_xZrNb_2O_8$ ($0 \leqslant x \leqslant 0.1$)ceramics

H.L. Pan, Q.Q. Liu, Y.H. Zhang, H.T. Wu*

School of Materials Science and Engineering, University of Jinan, Jinan 250022, China

Abstract: Wolframite structure $Zn_{1-x}Co_xZrNb_2O_8$ (x = 0, 0.02, 0.04, 0.06, 0.08, 0.10) ceramics were prepared by the conventional solid state method. The crystal structures were studied via X-ray diffraction, and lattice vibrational modes were obtained by Raman spectra. It could be found that all the A-site (Zn^{2+}/Co^{2+}, Zr^{4+}) and B-site (Nb^{5+}) cations were octahedrally coordinated with oxygen anions from the diagrammatic sketch of the crystal structure. Rietveld refinement was used to analyze the crystal structure and the lattice parameters were obtained. Based on the complex chemical bond theory and lattice parameters, intrinsic factors such as the bond ionicity, lattice energy, bond energy and coefficient of the thermal expansion were calculated. Based on the results, Nb-O bonds played an important role in affecting the microwave dielectric proprieties of $Zn_{1-x}Co_xZrNb_2O_8$ ceramics. Co^{2+} substitution would affect the crystal structure and influence the microwave dielectric properties. The tendency of the dielectric constant (ε_r) could be predicted by the polarizability and bond ionicity of Nb-O bonds, and the ε_r showed the same tendency with Raman shifts of Nb-O vibration modes. The variation of the quality factor ($Q{\cdot}f$) could be explained by the change of the lattice energy of Nb-O bonds and the full width at half maximum (FWHM) values of Nb-site Raman modes. The temperature coefficient of resonant frequency (τ_f) showed the same tendency with the bond energy, octahedral distortion and bond valence of Nb-O bonds, and the opposite tendency with the thermal expansion coefficient.

Keywords: $Zn_{1-x}Co_xZrNb_2O_8$; Rietveld refinement; Microwave dielectric properties; Raman spectra; Complex chemical bond theory;

*Corresponding author.
Tel.: +86 531 82765473; fax: +86 531 87974453.
E-mail address: mse_wuht@ujn.edu.cn (H.T. Wu).

View Article Online
DOI: 10.1039/C6RA20197K

1. Introduction

With the rapid development of the wireless and mobile communication systems, microwave dielectric materials have been widely applied in microwave components such as antennas, resonators and filters [1, 2]. As the core materials, microwave dielectric ceramics should meet three critical characteristics, a high dielectric constant (ε_r) to reduce the size of the components, a high quality factor ($Q{\cdot}f$) to increase the frequency selectivity and a near zero temperature coefficient of resonant frequency (τ_f) to guarantee the high temperature stability [3, 4]. Many microwave dielectric ceramics with high performance have been reported, which might be an interesting candidate for microwave application [5-7]. Among various dielectric compositions, $ZnZrNb_2O_8$ compound with monoclinic wolframite structure has attracted increasing attentions due to its good microwave dielectric properties [8-13]. Liao *et al.* [8] reported that $ZnZrNb_2O_8$ ceramics exhibited the microwave dielectric properties of ε_r = 30, $Q{\cdot}f$ = 61,000 GHz and τ_f = -52 ppm/°C for the first time. Subsequently, Ramarao *et al.* [9] investigated the correlations between the crystal structure and microwave dielectric properties of $AZrNb_2O_8$ (A = Mn, Mg, Zn and Co) ceramics. Ramarao *et al.* also reported that $ZnZrNb_2O_8$ ceramics possessed the microwave dielectric properties of ε_r = 16.5, $Q{\cdot}f$ = 53,400 GHz and τ_f = -49.8 ppm/°C. In addition, Li *et al.* [10, 11] investigated the effects of the ions substitution on the microwave dielectric properties of $ZnZrNb_2O_8$ ceramics and established the relationships that the $Q{\cdot}f$ and τ_f were correlated with the packing fraction and B-site bond valence, respectively. Zhang *et al.* calculated the parameters of the intrinsic factors such as the chemical bond ionicity, lattice energy and coefficient of thermal expansion using the generalized P-V-L theory and researched the connections between these parameters and microwave dielectric properties [12]. With the increasing of the Ta/Sb content, the variations of the ε_r, $Q{\cdot}f$ and τ_f showed the similar tendency with the bond ionicity, lattice energy and bond energy of the Nb-O bonds in $ZnZr(Nb_{1-x}Ta/Sb_x)_2O_8$, respectively.

In our previous research [13], the crystal structure of $AZrNb_2O_8$ (A = Zn, Co, Mg, Mn) changed with the variations of A-site ions, which could affect the Nb-O octahedrons. With the increasing of the A-site ions radius, the variations of the ε_r, $Q{\cdot}f$ and τ_f showed the linear relations with the polarizability, packing fraction and B-site octahedral distortion, respectively. However, a few of studies were reported about the influences of the Co^{2+} substitution in Zn-site on the microwave dielectric properties. The relationships between the intrinsic factors such as the bond ionicity, lattice energy, bond energy and coefficient of thermal expansion, and the microwave dielectric properties in $Zn_{1-x}Co_xZrNb_2O_8$ (x = 0,

View Article Online
DOI: 10.1039/C6RA20197K

0.02, 0.04, 0.06, 0.08, 0.10) have not been reported. The radius of Co^{2+} (0.745 Å, CN = 6) was similar to Zn^{2+} (0.74 Å, CN = 6) and a small amount of the substitution of Zn^{2+} by Co^{2+} could effectively adjust the B-site (B = Nb) octahedral distortion without detrimental effect on the phase compositions. Now in this work, firstly, $Zn_{1-x}Co_xZrNb_2O_8$ (x = 0, 0.02, 0.04, 0.06, 0.08, 0.10) ceramics were successfully prepared by the conventional solid state method. Secondly, the correlations among the phase compositions, sintering characteristics, micro-structures and microwave dielectric properties were systematically investigated. Moreover, intrinsic factors such as the bond ionicity, lattice energy, bond energy and coefficient of thermal expansion were calculated using the generalized P-V-L theory based on the results of the crystalline structure refinement. The structural parameters such as the bond valence, polarizability and octahedral distortion were calculated. Raman spectra were also used to investigate the structure through the peak shifts and FWHM of different vibration modes. Finally, the relationships among the microwave dielectric properties, intrinsic factors and structural parameters were systematically studied, respectively.

2. Experimental procedure

High purity oxide ZnO (99.9%, Aladdin), Nb_2O_5 (99.9%, Aladdin), CoO (99%, Ourchem) and ZrO_2 (99.99%, Aladdin) were used as raw materials to prepare $Zn_{1-x}Co_xZrNb_2O_8$ (x = 0, 0.02, 0.04, 0.06, 0.08, 0.10) ceramics through the conventional solid state method. Firstly, chemical powders were weighed according to the stoichiometric ratio and milled in a teflon jar with ZrO_2 balls as the medium. The slurry was then dried in an oven at the temperature of 80 °C. Secondly, the mixed powders were calcined at 1000 °C and then re-milled for 6 h. Thirdly, the powders were mixed with the paraffin wax as a binder and pressed into pellets with 10 mm in diameter and 5 mm in thickness at a pressure of 200 MPa. Finally, these pellets were sintered at 1050-1250 °C for 4 h in air at a heating rate of 5 °C/min.

Phase analysis of the samples was conducted with the help of a Rigaku diffractometer (Model D/MAX-B, Rigaku Co., Japan) using Cu Kα radiation (λ=0.1542 nm) at 40 kV and 40 mA settings. Rietveld refinement was operated using Fullprof software. The reliability of the results was judged by the pattern R factor (Rp), weighted pattern R factor (Rwp) and goodness of fit indicator ($\chi 2$). Raman spectra of the samples was collected using the high resolution Raman spectrometer (LobRAM HR Evolution, HORIBA Jobin Yvon S.A.S.). The surface morphology was studied by scanning electron microscopy (Model JEOL JEM-2010, FEI Co., Japan). A network analyzer (N5234A, Agilent Co., America) was used to measure the microwave dielectric properties of the samples. The dielectric

View Article Online
DOI: 10.1039/C6RA20197K

constant was measured using Hakki-Coleman post-resonator method using an electric probe suggested by Hakki and Coleman [14]. The unloaded quality factors were measured using the TE01d mode by the cavity method [15]. All the measurements were conducted at room temperature in the frequency regions of 8-12 GHz. The temperature coefficients of resonant frequency were measured in the temperatures range of 25-85 °C and calculated using the Equ. (1).

$$\tau_f = \frac{f_2 - f_1}{f_1(T_2 - T_1)} \quad (1)$$

Where f_1 is the resonant frequency at the temperature of T_1 and f_2 at the temperature of T_2.

The apparent density of samples was measured using Archimedes method (Mettler Toledo XS64). To obtain the relative density of samples, the theoretical density was calculated through the cell parameters and atomic weight [16] using Equ. (2).

$$\rho_{\text{theory}} = \frac{ZA}{V_C N_A} \quad (2)$$

Where Z, A, V_C and N_A are the number of atoms in the unit cell, all the atomic weights in the unit cell, the volume of the unit cell and Avogadro constant, respectively. The relative density was obtained using Equ. (3).

$$\rho_{\text{relative}} = \frac{\rho_{\text{apparent}}}{\rho_{\text{theory}}} \times 100\ \% \quad (3)$$

3. Results and discussion

3.1 Single phase refinement

Fig. 1 showed the XRD patterns of $Zn_{1-x}Co_xZrNb_2O_8$ (x = 0, 0.02, 0.04, 0.06, 0.08, 0.10) ceramics sintered at 1150 °C. All the diffraction peaks well matched with the monoclinic structure $ZnZrNb_2O_8$ (JCPDS No. 48-0324) with the space group of p2/c and no other phases were observed. With the increasing of the Co^{2+} substitution, the X-ray diffraction patterns did not significant change. $CdWO_4$ reported by Daturi *et al.* [17] was adopted as the starting model of Rietveld refinement. Some parameters such as the zero point, background, half width, asymmetry parameters, unit-cell parameters, atomic position, *etc.* were refined gradually using Fullprof software. The typical refinement patterns of $Zn_{1-x}Co_xZrNb_2O_8$ samples with different Co^{2+} substitution were illustrated in Fig. 2. The calculated pattern was overlaid on the measured pattern and the differences between two profiles were plotted along the bottom. It was found that the measured patterns fitted well with the calculated patterns with the structure of $CdWO_4$. The atomic positions and occupations of $Zn_{0.94}Co_{0.06}ZrNb_2O_8$ were given in

View Article Online
DOI: 10.1039/C6RA20197K

Table 1. The lattice parameters, Rp values, Rwp values and *χ2* values of the $Zn_{1-x}Co_xZrNb_2O_8$ were shown in Table 2, which was used to calculate the bond length of cation-oxygen bonds shown in Table 3 and other parameters.

3.2 Crystal structure

Based on the lattice parameters, atomic positions and occupations, schematic representations of the $Zn_{1-x}Co_xZrNb_2O_8$ (2×2×2) supercell, and the A-site (A = Zn^{2+}/Co^{2+}, Zr^{4+}) and B-site (B = Nb^{5+}) oxygen octahedrons of the $Zn_{0.94}Co_{0.06}ZrNb_2O_8$ with the bond lengths were shown in Fig. 3. The sketch map of the crystal structure showed that $ZnZrNb_2O_8$ were constituted by the A-site (A = Zn^{2+}/Co^{2+}, Zr^{4+}) and B-site (B = Nb^{5+}) oxygen octahedrons. In this structure, the A-site (Zn^{2+}/Co^{2+}, Zr^{4+}) and B-site (Nb^{5+}) cations occupied *2f* and *2e* Wyckoff positions, respectively. The two different oxygen anions occupied the *4g* Wyckoff positions. Oxygen O1 was connected to one B-site (Nb^{5+}) cation and two A-site (Zn^{2+}/Co^{2+}, Zr^{4+}) cations and another oxygen O2 was bonded with one A-site (Zn^{2+}/Co^{2+}, Zr^{4+}) and two B-site (Nb^{5+}) cations.

The bond types and their bond lengths of $Zn_{1-x}Co_xZrNb_2O_8$ ceramics were illustrated in Table 3. According to the results of Fig. 3 and Table 3, it could be found that Co^{2+} substitution would change the oxygen octahedrons. Based on the results of the bond lengths, the values of the octahedron distortions could be calculated using Equ. (4) [18] and the results were shown in Table 4.

$$\delta_{\text{octahedron}} = \frac{\text{B-O distance}_{\max} - \text{B-O distance}_{\min}}{\text{B-O distance}_{average}} \quad (4)$$

The calculated results were in the range of 10%-26%. With the increasing of the Co^{2+} substitution from 0% to 10%, both the A-site and B-site octahedral distortion showed significant changes and the values of the B-site octahedrons were big than A-site octahedrons, which would have an potential effects on the microwave dielectric properties of $Zn_{1-x}Co_xZrNb_2O_8$ ceramics. The bond valence of all the oxygen octahedrons was calculated as follows and the results were also shown in Table 4 [19].

$$V_{ij} = \sum v_{ij} \quad (5)$$

$$v_{ij} = \exp\left(\frac{R_{ij} - d_{ij}}{b'}\right) \quad (6)$$

Where V_{ij} represented the sum of all the bond valences, R_{ij} indicated the bond valence parameter, d_{ij} indicated the length of a bond between atoms i and j, and b' indicated an universal constant equal to 0.37.

Raman spectra of $Zn_{1-x}Co_xZrNb_2O_8$ ceramics sintered at 1150 °C were shown in Fig. 4(a). The

View Article Online
DOI: 10.1039/C6RA20197K

solid solutions possessed the wolframite structure with P2/c space group and C_{2h} (2/m) point group. Based on the group theoretical calculations, 39 vibrational modes were predicted for $ZnZrNb_2O_8$ compositions and the irreducible representation of all these modes (Acoustic and Optic modes: $\Gamma = 9A_g + 8A_u + 12B_g + 10B_u$) was given [20]. Among of these modes, Infrared active modes were $8A_u + 10B_u$ and Raman active modes were $9A_g + 12B_g$. Where all the 'g' vibrations were the Raman active modes, whereas 'u' vibrations were the IR active modes [13]. As shown in Fig. 4(a), ten vibration modes were observed and some vibration modes were not detected because of their weak vibration characteristics. Every peak corresponded to a specified form vibration mode. 122 cm^{-1}, 190 cm^{-1} and 413 cm^{-1} corresponded to the lattice vibration, the Zr-O stretching vibration and the Zr-O stretching vibration, respectively [21]. In addition, it was founded that the significant Raman active modes existed in the high frequency range (1000-800 cm^{-1}). According to the results reported by Murthy *et al.* and Daturi *et al.*, the deconvoluted Raman spectra of the $Zn_{0.94}Co_{0.06}ZrNb_2O_8$ ceramic were shown in Fig. 4(b), it could be speculated that the higher intensity mode at nearly 875 cm^{-1} was symmetric stretching vibrations of the Nb-O bonds, and nearly 840 cm^{-1} was the asymmetric stretching vibrations of Nb-O bonds [22-24].

Raman modes were very sensitive to the nature of the chemical bond and the distribution of cations at respective Wyckoff sites. At A-site, Zn^{2+} cations instead by Co^{2+} cations could affect the distorted degree of the octahedron and cause the shifts of Raman modes in $Zn_{1-x}Co_xZrNb_2O_8$ ceramics. The distribution of cations at different sites were also responsible for the full width at half maximum (FWHM) of the Raman modes [23]. Thus, it could be considered that the Raman shifts and FWHM of the different compositions had relationships with the microwave dielectric properties. For example, Shi *et al.* reported the correlations between the vibrational modes and structural characteristics of $Ba[(Zn_{1-x}Mg_x)_{1/3}Ta_{2/3}]O_3$ ceramics. FWHM values of three Raman modes were related to the tilting of the oxygen octahedrons and indirectly affected the quality factor of the ceramics [25]. In our previous research, the changes of the cation-oxygen bond lengths and the different cations substitution at A-sites of the $AZrNb_2O_8$ (A = Zn, Co, Mg, Mn) ceramics caused Raman shifts of A_g mode in nearly 840 cm^{-1} [13]. In order to investigate the influences of the Co^{2+} substitution on the Raman shifts and the FWHM of the vibration modes, all the modes of $Zn_{1-x}Co_xZrNb_2O_8$ ceramics were shown in Table 5 and Table 6. With the increasing of the x values, it could be observed that the asymmetric stretching vibrations of Nb-O bonds were shifted from 843.8181 cm^{-1} to 839.4265 cm^{-1}, which indicated that changes in the

View Article Online
DOI: 10.1039/C6RA20197K

cation-oxygen bond lengths might be responsible for the shifts of Raman modes A_g in nearly 840 cm^{-1}. In addition, FWHM values of the vibration modes were obtained from the Lorentz fitting. The values of the Raman modes A_g in nearly 840 cm^{-1} fluctuated from 51.0018 to 33.4567, which related to the microwave dielectric properties [22, 23].

3.3 Sintering characteristics and micromorphology

The apparent densities of the $Zn_{1-x}Co_xZrNb_2O_8$ (x = 0, 0.02, 0.04, 0.06, 0.08, 0.10) ceramics as a function of the sintering temperatures were given in Fig. 5(a). With the sintering temperatures increasing from 1050 °C to 1250 °C, the apparent densities of the samples increased and the maximum apparent density were obtained at 1150 °C. Based on the lattice parameters and atomic weight, the theoretical density and relative density could be calculated. These results were shown in Table 4. The variations of the relative density for ceramics sintered at 1150 °C were shown in Fig. 5(b). With the increasing of the Co^{2+} displacement, the relative densities had no obvious change. It could be also found that the relative densities of all the samples were close to 95%, which meant that the samples possessed the nearly full density at the sintering temperature of 1150 °C.

SEM micrographs of $Zn_{1-x}Co_xZrNb_2O_8$ (x = 0, 0.02, 0.04, 0.06, 0.08, 0.10) sintered at 1150 °C were illustrated in Fig. 6. Single phase $ZnZrNb_2O_8$ possessed the smaller grains. With the increasing of the x values, the grain size increased obviously and there were no significant changes in the grain size each other. The sizes of the grains were in the range of 3-8 um, and the grains showed homogeneous, which indicated that nearly dense micro-structure of the $Zn_{1-x}Co_xZrNb_2O_8$ ceramics could be obtained at 1150 °C.

3.4 Complex bond theory and bond energy calculation

Microwave dielectric properties dependent on both extrinsic factors and intrinsic factors. Density, impurity, secondary phase and grain sizes played an important role in extrinsic factors, while the intrinsic factors were mainly affected by the crystal structure and lattice defects [26-28]. In our researches, a dense state was obtained for $Zn_{1-x}Co_xZrNb_2O_8$ ceramics and no other secondary phases were found at the sintering temperature of 1150 °C, which meant that the extrinsic factors could be ignored. Thus, intrinsic factors such as the bond ionicity, lattice energy, bond energy and coefficient of thermal expansion should be considered. Kapustinskii *et al.* and Xue *et al.* reported that the ionicity of chemical bond could explain many basic properties in diverse areas [29, 30], which could be evaluated by P-V-L theory. Zhang *et al.* improved the P-V-L theory and made it possible for applications in

View Article Online
DOI: 10.1039/C6RA20197K

complex crystals [31-33]. Based on the crystallographic data shown in Table 2 and the complex chemical bond theory, the complex crystals $Zn_{1-x}Co_xZrNb_2O_8$ were decomposed into the sum of binary crystals as follows.

$$\begin{aligned}
&Zn_{1-x}Co_xZrNb_2O_8=2ANbO_4\\
&=2(A_{1/3}O(1)_{2/3}+A_{2/3}O(2)_{4/3}+Nb_{2/3}O(1)_{4/3}+Nb_{1/3}O(2)_{2/3})\\
&=2(A_{1/3}O(1)_{2/3}+A_{1/3}O(2)_{2/3}{}^{1}+A_{1/3}O(2)_{2/3}{}^{2}+Nb_{1/3}O(1)_{2/3}{}^{1}\\
&+Nb_{1/3}O(1)_{2/3}{}^{2}+Nb_{1/3}O(2)_{2/3})\\
&=Zn/Co_{1/3}O(1)_{2/3}+Zn/Co_{1/3}O(2)_{2/3}{}^{1}+Zn/Co_{1/3}O(2)_{2/3}{}^{2}\\
&+Zr_{1/3}O(1)_{2/3}+Zr_{1/3}O(2)_{2/3}{}^{1}+Zr_{1/3}O(2)_{2/3}{}^{2}\\
&+Nb_{2/3}O(1)_{4/3}{}^{1}+Nb_{2/3}O(1)_{4/3}{}^{2}+Nb_{2/3}O(2)_{4/3}
\end{aligned} \tag{7}$$

Fig. 7 showed the coordination number and the charge distribution of ions in the $Zn_{1-x}Co_xZrNb_2O_8$. The coordination numbers of Zn/Co, Zr, Nb, O(1), O(1) were 6, 6, 6, 3, 3, respectively. The valence electron numbers of cations in these bonds were $Z_{Zn/Co}=2$, $Z_{Zr}=4$ and $Z_{Nb}=5$, while the effective valence electron numbers of anions were $Z_O=-1$ in the Zn/Co-O bond, $Z_O=-2$ in the Zr-O bond and $Z_O=-2.5$ in the Nb-O bond. The difference effective valence electron numbers of the oxygen atom were mainly dependent on the charge balance for each sub-formula.

According to the generalized P-V-L theory [31-33], the bond ionicity of an individual bond μ could be calculated as follows.

$$f_i=\frac{(C^\mu)^2}{(E_g^\mu)^2} \tag{8}$$

$$(E_g^\mu)^2=(E_h^\mu)^2+(C^\mu)^2 \tag{9}$$

$$(E_h^\mu)^2=\frac{39.74}{(d^\mu)^{2.48}} \tag{10}$$

$$C^\mu=14.4b^\mu\exp(-k_s^u r_0^\mu)[(Z_A^u)^*-\frac{n}{m}(Z_B^u)^*]/r_0^\mu \tag{11}$$

Where E_g^μ was the average energy gap for the bond μ and it could be composed into homopolar E_h^μ and heteropolar C^μ parts. Some parameters such as $\exp(-k_s^u r_0^\mu)$ and b^μ in Equ. 11 could be obtained in reference [34]. The calculated results of the bond ionicity were listed in Table 7. The average bond ionicities $Af_{i(A\text{-}O)}$ of $Zn_{1-x}Co_xZrNb_2O_8$ (x = 0, 0.02, 0.04, 0.06, 0.08, 0.10) ceramics sintered at 1150 °C as a variation of A-O bonds were shown in Fig. 8(a). Associated with the calculated

View Article Online
DOI: 10.1039/C6RA20197K

results, it was found that the average values of the bond ionicity $Af_{i(Zn/Co-O)}$, $Af_{i(Zr-O)}$ and $Af_{i(Nb-O)}$ were 0.6399, 0.8046 and 0.8385, respectively. Based on the result of $Af_{i(Zn/Co-O)}<Af_{i(Zr-O)}<Af_{i(Nb-O)}$, the average bond ionicity $Af_{i(Nb-O)}$ could be predominant contribution to the dielectric constant in $Zn_{1-x}Co_xZrNb_2O_8$ ceramics.

As for the lattice energy, the parameters of a single bond could also be separated into ionic and covalent parts. Based on the generalized P-V-L theory [31-33], the lattice energy U of the $Zn_{1-x}Co_xZrNb_2O_8$ crystal was calculated by Equs. (12-15).

$$U = \sum_{\mu} U_b^{\mu} \tag{12}$$

$$U_b^{\mu} = U_{bc}^{\mu} + U_{bi}^{\mu} \tag{13}$$

$$U_{bc}^{\mu} = 2100m \frac{(Z_+^{\mu})^{1.64}}{(d^{\mu})^{0.75}} f_C^{\mu} \tag{14}$$

$$U_{bi}^{\mu} = 1270 \frac{(m+n)Z_+^{\mu}Z_-^{\mu}}{d^{\mu}} (1 - \frac{0.4}{d^{\mu}}) f_i^{\mu} \tag{15}$$

Where U_{bc}^{μ} was the covalent part and U_{bi}^{μ} was the ionic part of μ bond. Z_+^{μ} and Z_-^{μ} were the valence states of the cation and the anion which constituted the μ bond. The calculated results of the lattice energies were listed in Table 8. The average lattice energies $AU_{(A-O)}$ of $Zn_{1-x}Co_xZrNb_2O_8$ (x = 0, 0.02, 0.04, 0.06, 0.08, 0.10) ceramics sintered at 1150 °C as a variation of the A-O bonds were shown in Fig. 8(b). For $Zn_{1-x}Co_xZrNb_2O_8$ ceramics, the average values of the lattice energies $AU_{(Zn/Co-O)}$, $AU_{(Zr-O)}$ and $AU_{(Nb-O)}$ were 1076, 3910 and 12546 kJ/mol, respectively. Obviously, there was the sequence of $AU_{(Zn/Co-O)}<AU_{(Zr-O)}<AU_{(Nb-O)}$, the lattice energy of $U_{(Nb-O)}$ could be predominant contribution to $Q \cdot f$ value as intrinsic factors in the $Zn_{1-x}Co_xZrNb_2O_8$ ceramics.

It was known that the shorter bond length correlated with the higher bond energy, which indicated that the crystal structure would be more stabilization. Sanderson reported that the bond energy could be obtained by the chemical bond and electronegativity [35, 36]. Based on the electronegativity and complex chemical bond theory, the bond energy E of a complex crystal could be written as Equs. (16-19).

$$E = \sum_{\mu} E_b^{\mu} \tag{16}$$

Where E_b^{μ} was the bond energy of the μ bond, which was composed of nonpolar covalence energy E_c^{μ} and complete ionicity energy E_i^{μ} parts as as follows.

View Article Online
DOI: 10.1039/C6RA20197K

$$E_b^{\mu} = t_c E_c^{\mu} + t_i E_i^{\mu} \quad (17)$$

$$E_i^{\mu} = \frac{33200}{d^{\mu}} \quad (18)$$

For any binary A_mB_n compounds, the nonpolar covalence energy E_c^{μ} parts could be calculated as shown in Equ. 19.

$$E_c^{\mu} = \frac{(r_{cA} + r_{cB})}{d^{\mu}} (E_{A-A} E_{B-B})^{1/2} \quad (19)$$

Where r_{cA} and r_{cB} were the covalent radii, $E_{A\text{-}A}$ and $E_{B\text{-}B}$ were the homonucler bond energy. In this paper, $E_{Zn\text{-}Zn}$=22.2 kJ mol^{-1}, $E_{Co\text{-}Co}$=127 kJ mol^{-1}, $E_{Zr\text{-}Zr}$=298.2 kJ mol^{-1}, $E_{Nb\text{-}Nb}$=513 kJ mol^{-1} and $E_{O\text{-}O}$=498.36 kJ mol^{-1}, which could be obtained from the handbook [37]. The calculated results of the bond energy were listed in Table 9. The average bond energies $AE_{(A\text{-}O)}$ of $Zn_{1-x}Co_xZrNb_2O_8$ (x = 0, 0.02, 0.04, 0.06, 0.08, 0.10) ceramics sintered at 1150 °C as a variation of A-O bonds were shown in Fig. 8(c). Associated with the results, it was found that the average bond energies were 266.5329 KJ/mol for $AE_{(Zn/Co\text{-}O)}$, 490.6615 KJ/mol for $AE_{(Zr\text{-}O)}$ and 582.1704 KJ/mol for $AE_{(Nb\text{-}O)}$. Based on the sequence of $AE_{(Zn/Co\text{-}O)}<AE_{(Zr\text{-}O)}<AE_{(Nb\text{-}O)}$, the bond energy $E_{(Nb\text{-}O)}$ made predominant contribution to the τ_f of $Zn_{1-x}Co_xZrNb_2O_8$ ceramics.

Based on the complex chemical bond theory, the coefficient of thermal expansion α could be written as the following Equ. (20).

$$\alpha = \sum_{\mu} F_{mn}^{\mu} \alpha_{mn}^{\mu} \quad (20)$$

Where F_{mn}^{μ} was the proportion of μ bond in the total bonds of a supercell. For any binary A_mB_n compounds, the coefficient of thermal expansion α_{mn}^{μ} could be calculated as the following Eqs. (21-23).

$$\alpha_{mn}^{\mu} = -3.1685 + 0.8376\ \gamma_{mn} \quad (21)$$

$$\gamma_{mn} = \frac{kZ_A^{\mu} N_{CA}^{\mu}}{U_b^{\mu} \Delta_A} \beta_{mn} \quad (22)$$

$$\beta_{mn} = \frac{m(m+n)}{2n} \quad (23)$$

Where k was Boltzmann constant, Z_A^{μ} was the valence states of cation, N_{CA}^{μ} was the coordination number of μ bond for cation A. The calculated results of the coefficient of the thermal expansion were listed in Table 10. The average coefficient of thermal expansion $A\alpha_{(A\text{-}O)}$ of $Zn_{1-x}Co_xZrNb_2O_8$ (x = 0,

View Article Online
DOI: 10.1039/C6RA20197K

0.02, 0.04, 0.06, 0.08, 0.10) ceramics sintered at 1150 °C as a variation of A-O bonds were shown in Fig. 8(d). The Nb-O and Zr-O bonds showed the excellent stable coefficient of thermal expansion of 2.1921 and 4.2116, while the bond of Zn/Co-O showed the obvious coefficient of thermal expansion of 10.2414. Based on the result of $A\alpha_{(Nb\text{-}O)}<A\alpha_{(Zr\text{-}O)}<A\alpha_{(Zn/Co\text{-}O)}$, temperature coefficient of resonant frequency τ_f would mainly be affected by the coefficient of the thermal expansion of Nb-O bonds.

Based on the cell parameters and complex chemical bond theory, the bond ionicity, lattice energy, bond energy and coefficient of thermal expansion were calculated to evaluate the structural characteristics. According to the results, It could be found that the Nb-O bonds played an important role in affecting the microwave dielectric proprieties of $Zn_{1-x}Co_xZrNb_2O_8$. In the following, the relationships between the microwave dielectric properties and intrinsic factors of Nb-O bonds were researched, and the connections between the microwave dielectric properties and structural parameters of Nb-O bonds were also studied. In addition, the relationships among the microwave dielectric properties, Raman shifts and FWHM of Nb-O bonds were researched.

3.5 Microwave dielectric properties characterization

The dielectric constants of $Zn_{1-x}Co_xZrNb_2O_8$ (x = 0, 0.02, 0.04, 0.06, 0.08, 0.10) ceramics sintered at the temperatures range of 1050 °C-1250 °C were illustrated in Fig. 9(a). With the sintering temperatures increasing from 1050 °C to 1250 °C, the ε_r values gradually increased and achieved maximum at 1150 °C. It was well known that the ε_r values of ceramics were dependent on the extrinsic factors such as density, porosity, secondary phase and intrinsic parameters such as the polarizability, distortion of the oxygen octahedron [38, 39]. In our research, the variation of the ε_r values exhibited the same tendency with the apparent densities shown in Fig. 5(a). When the ceramics possessed the relative density about 95% and no other secondary phases were obtained at the sintering temperature of 1150 °C, the polarizability played a major role in the variation of the dielectric constants. The dielectric constants of the $Zn_{1-x}Co_xZrNb_2O_8$ ceramics sintered at 1150 °C were illustrated in Fig. 9(b). With the x values increasing from 0 to 0.1, the ε_r values decreased due to that the polarizability of Co^{2+} (1.65 $Å^3$) was smaller than Zn^{2+} (2.04 $Å^3$). To clarify the effects of the crystal structure on the dielectric constant of $Zn_{1-x}Co_xZrNb_2O_8$ ceramics, theoretical dielectric polarizability ($\alpha_{theo.}$) of the samples were calculated according to the additive rule as formulated in Equ. 24 [40]. While the observed dielectric polarizability ($\alpha_{obs.}$) was calculated by the generalized Clausius-Mossotti equation as formulated in Equ. 25 with the measured dielectric constant at microwave frequencies [41].

View Article Online
DOI: 10.1039/C6RA20197K

$$\alpha_{theo.}(Zn_{1-x}Co_xZrNb_2O_8) = (1-x)\alpha(Zn^{2+}) + x\alpha(Co^{2+}) + \alpha(Zr^{4+}) + 2\alpha(Nb^{5+}) + 8\alpha(O^{2-}) \quad (24)$$

$$\alpha_{obs.} = \frac{1}{b}V_m\frac{\varepsilon-1}{\varepsilon+2} \quad (25)$$

Where $\alpha\ (Zn^{2+})$=2.04 Å^3, $\alpha\ (Co^{2+})$=1.65 Å^3, $\alpha\ (Nb^{5+})$=3.97 Å^3, $\alpha\ (O^{2-})$=2.01 Å^3, and $\alpha\ (Zr^{4+})$=3.25 Å^3 reported by Shannon [41]. Moreover, V_m, ε and b indicated the molar volume of samples, dielectric constant and constant value (4π/3), respectively. The variations of the $\alpha_{theo.}$ and the $\alpha_{obs.}$ were also shown in Fig. 9(b). It could be found that the variation of the ε_r values showed the similar tendency with the $\alpha_{theo.}$ and $\alpha_{obs.}$ values. By comparison, it could be found that the $\alpha_{theo.}$ and $\alpha_{obs.}$ were in good agreement with each other. The minor deviation could attribute to the relative density because the $\alpha_{obs.}$ values were dependent on the specimens and fabrication process.

Fig. 8(a) showed that the bond ionicity of Nb-O bonds played major effects on the dielectric constants of $Zn_{1-x}Co_xZrNb_2O_8$ ceramics and the variation of the bond ionicity could be used to predict the tendency of ε_r values. As shown in Table 7, the values of $Af_{i\ (Nb-O)}$ were 84.0001, 83.9464, 84.0604, 83.9184, 83.6496, 83.5463 with the x increasing from 0 to 0.1. Thus, it could be concluded that Co^{2+} substitution affected the bond ionicity of the Nb-O bonds. As shown in Fig. 9(c), with the x increasing from 0 to 0.1, the change of the average ionicity of Nb-O bonds showed the similar tendency with the dielectric constants, which was also reported by other reports [12, 13]. In addition, as the radius of A-site ions decreased from Zn^{2+} to Co^{2+}, the Raman shifts of modes in nearly 840 cm^{-1} were sensitive and move to the lower wave number as shown in Fig. 9(c). The Redshift of the stretching vibrations in Nb-O bonds also indicated the lower ionic polarizability, which agreed with other reports [42, 43].

It was reported that the *Q·f* values were affected by the intrinsic factors and extrinsic factors [38, 39]. The extrinsic factors were the second phases, grain sizes and the densification, and the intrinsic factors were the crystal structure and lattice vibration. As shown in Fig. 10(a), with the sintering temperatures increasing from 1050 to 1250 °C, the *Q·f* values of $Zn_{1-x}Co_xZrNb_2O_8$ gradually increased and reached the maximum values at 1200 °C. The remarkable increase of Q·*f* values under 1200 °C was explained by the reduction of the porosity according to the results of apparent densities shown in Fig. 5(a), and the abnormal grain growth might led to the reduce of *Q·f* values above 1200 °C. When the ceramics possessed the relative density about 95% and no other secondary phases were obtained at the sintering temperature of 1150 °C, the *Q·f* values were mainly affected by the intrinsic factors.

The lattice energy was an appropriate physical quantity to quantitatively evaluate the lattice

View Article Online
DOI: 10.1039/C6RA20197K

vibration and phase stability of a complex crystal structure. Therefore, the concept of the lattice energy could be applied to analyze the variation of $Q \cdot f$ values in $Zn_{1-x}Co_xZrNb_2O_8$ systems [12, 13]. the average lattice energy of Nb-O bonds for $Zn_{1-x}Co_xZrNb_2O_8$ ceramics were shown in Fig. 10(c). It was clarified that the lattice energy of Nb-O bonds possessed a higher value in $Zn_{1-x}Co_xZrNb_2O_8$ ceramics and the $Q \cdot f$ values were strongly dependent on the lattice energy. With the increasing of the x values, the average U_{Nb-O} values and $Q \cdot f$ values showed the same increasing tendency, which was similar to other reports [12, 13]. For example, Zhang *et al.* reported the average U_{Nb-O} values were proportional to the $Q \cdot f$ values of the $ZnZr(Nb_{1-x}Ta/Sb_x)_2O_8$ ceramics [12]. They also reported the similar tendency in $NdNbO_4$ systems [34, 44]. In addition, with the increasing of the x values, the variation of the Raman FWHM values around 840 cm^{-1} showed the opposite tendency with the $Q \cdot f$ values, which agreed with the results reported by shi *et al.* [42, 43].

Fig. 11 illustrated the relationships among the temperature coefficient of resonant frequency (τ_f), bond energy (E), thermal expansion coefficient (α), octahedral distortion (δ) and bond valence (V) of $Zn_{1-x}Co_xZrNb_2O_8$ ceramics sintered at 1150 °C with the different amount of Co^{2+} contents. With the x values increasing from 0 to 0.1, the τ_f values of $Zn_{1-x}Co_xZrNb_2O_8$ ceramics gradually increased from -42.68 to -7.48 ppm/°C. In general, the τ_f value was related to the temperature coefficient of dielectric constant (τ_ε) and coefficient of thermal expansion (α) shown in Equ. 26.

$$\tau_f = -\alpha - \frac{1}{2}\tau_\varepsilon \tag{26}$$

Although the linear thermal expansion coefficient (α) was considered of 10 ppm/°C for all the ceramics [45], it was considered that the α values of Nb-O bonds played an important role in $Zn_{1-x}Co_xZrNb_2O_8$ system. As shown in Fig. 11, with the Co^{2+} ions increasing, the α values of Nb-O bonds decreased from 2.2392 to 2.1578, which was inversely proportional to the τ_f values. Thus, the decrease of the thermal expansion coefficient of Nb-O bonds would improve the temperature stability of $Zn_{1-x}Co_xZrNb_2O_8$ system.

As for temperature coefficient of dielectric constant (τ_ε), the values could be derived according to Clausius-Mosotti equation as follows.

$$\tau_\varepsilon = \frac{1}{\varepsilon_r}\left(\frac{\partial \varepsilon_r}{\partial T}\right) = \frac{(\varepsilon_r - 1)(\varepsilon_r + 2)}{3\varepsilon_r} \times \left[\frac{1}{\alpha_m}\left(\frac{\partial \alpha_m}{\partial T}\right)_V + \frac{1}{\alpha_m}\left(\frac{\partial \alpha_m}{\partial V}\right)_T \left(\frac{\partial V}{\partial T}\right)_P - \frac{1}{V}\left(\frac{\partial V}{\partial T}\right)_P\right] \tag{27}$$

Where α_m and V indicated the polarizability and volume of a small sphere, respectively. According to Bosman *et al.* [45], the second and third items in the square brackets were related to the volume

View Article Online
DOI: 10.1039/C6RA20197K

expansion, which possessed nearly equal value. Therefore, the effect of these terms could be ignored and the τ_ε was mainly dependent on the first part influenced by the crystal structure. Kim *et al.* reported that the distortion of the oxygen octahedral in [BO_6] showed a closely relation with τ_f. In addition, the bond valence between the cations and oxygen would affect the distortion of the oxygen octahedral [46]. As shown in Fig. 11, the τ_f values were shifted to the positive direction primarily depending on the increase of the bond valence of Nb-O bonds and oxygen octahedral distortion. In addition, the higher bond energy of Nb-O bonds correlated with the higher bond strength and more stable Nb-O octahedral structure. With the variation of Nb-site bond energy, both the bond valence and oxygen octahedral distortion of Nb-O bonds showed the increasing trend and resulted in the increase of the τ_f values. Thus, it was suggested that the distortion of the oxygen octahedral, bond valence, thermal expansion coefficient and bond energy were also key factors on the τ_f values.

4. Conclusion

$Zn_{1-x}Co_xZrNb_2O_8$ (x = 0, 0.02, 0.04, 0.06, 0.08, 0.10) ceramics were successfully prepared by the conventional solid state method. The effects of Co^{2+} substitution on the phase composition, micro-structure and microwave dielectric properties of $Zn_{1-x}Co_xZrNb_2O_8$ were discussed. Dense samples were obtained at 1150 °C and $Zn_{1-x}Co_xZrNb_2O_8$ possessed wolframite structure with p2/c space group. Intrinsic factors such as the bond ionicity, lattice energy, bond energy and coefficient of thermal expansion were calculated using the generalized P-V-L theory based on the results of the crystalline structure refinement. The structural parameters such as the bond valence, polarizability and octahedral distortion were calculated. Based on the results, Nb-O bonds played an important role in affecting the microwave dielectric proprieties of $Zn_{1-x}Co_xZrNb_2O_8$. The change of the dielectric constants showed the similar tendency with the polarizability, bond ionicity of the Nb-O bonds and Raman shifts of Nb-O vibration modes. The variation of the $Q \cdot f$ showed the similar tendency with the lattice energy of the Nb-O bonds, and the opposite tendency with the variation of Raman FWHM values of Nb-O bonds. As for the τ_f values, it could be concluded that the change of the τ_f values showed the similar tendency with the distortion of the oxygen octahedral, bond valence and bond energy, and the opposite tendency with the thermal expansion coefficient.

Acknowledgments

This work was supported by the National Natural Science Foundation (No. 51472108).

View Article Online
DOI: 10.1039/C6RA20197K

Reference

1. T. A. Vanderah, *Science*, 2002, **298**, 1182.

2. R. Freer and R. Azough, *J. Eur. Ceram. Soc.*, 2008, **28**, 1433.

3. J. Guo, D. Zhou, Y. Li, T. Shao, Z. M. Qi, B. B. Jin and H. Wang, *Dalton Trans.*, 2014, **43**, 11888.

4. D. Zhou, W. B. Li, L. X. Pang, Z. X. Yue, G. S. Pang and X. Yao, *RSC Adv.*, 2015, **5**, 19255.

5. D. Zhou, D. Guo, W. B. Li, L. X. Pang, X. Yao, D. W. Wang and I. M. Reaney, *J. Mater. Chem. C*, 2016, **4**, 5357.

6. D. Zhou, W. B. Li, H. H. Xi, L. X. Pang and G. S. Pang, *J. Mater. Chem. C*, 2015, **3**, 2582.

7. D. Zhou, L. X. Pang, J. Guo, Z. M. Qi, T. Shao, Q. P. Wang, H. D. Xie, X. Yao and C. A. Randall, *Inorg. Chem.*, 2014, **53**, 1048.

8. Q. W. Liao, L. X. Li, X. Ren, X. X. Yu, D. Guo and M. J. Wang, *J. Am. Ceram. Soc.*, 2012, **95**, 3363.

9. S. D. Ramarao and V. R. K. Murthy, *Scripta Mater.*, 2013, **69**, 274.

10. L. X. Li, S. Zhang, J. Ye, X. S. Lv, H. Sun and S. Li, *Ceram. Int.*, 2016, **42**, 9157.

11. J. Ye, L. X. Li, H. Sun, X. S. Lv, J. Y. Yu and S. Li, *J. Mater. Sci.: Mater. Electron.*, 2015, **26**, 8954.

12. P. Zhang, Y. G. Zhao and H. T. Wu, *Dalton. Trans.*, 2015, **44**, 16684.

13. H. T. Wu, Z. B. Feng, Q. J. Mei, J. D. Guo and J. X. Bi, *J.Alloys Comp.*, 2016, **648**, 368.

14. B. W. Hakki and P. D. Coleman, *IEEE Trans.*, 1960, **8**, 402.

15. W. E. Courtney, *IEEE Trans.*, 1970, **18**, 476.

16. E. S. Kim, C. J. Jeon and P. G. Clem, *J. Am. Ceram. Soc.*, 2012, **95**, 2934.

17. M. Daturi, G. Busca, M. M. Borel, A. Leclaire and P. Piaggio, *J. Phys. Chem. B*, 1997, **101**, 4358.

18. F. Lichtenberg, A. Herrnberger and K. Wiedenmann, *J. Solid State Chem.*, 2008, **36**, 253.

19. P. Zhang, Y. G. Zhao, J. Liu, Z. K. Song, X. Y. Wang and M. Xiao, *J. Alloys Compd.*, 2015, **640**, 90.

20. M. I. Aroyo, J. M. Perez-Mato, D. Orobengoa, E. Tasci, G. De La Flor and A. Kirov, *Bulg. Chem. Commun.*, 2011, **43**, 183.

21. Y. Zhang, Y. C. Zhang and M. Q. Xiang, *J. Eur. Ceram. Soc.*, 2016, **36**, 1945.

22. S. D. Ramarao and V. R. K. Murthy, *Phys. Chem. Chem. Phys.*, 2015, **17**, 12623.

23. S. D. Ramarao and V. R. K. Murthy, *Dalton Trans.*, 2015, **44**, 2311.

24. D. Zhou, L. X. Pang, H. Wang, J. Guo, X. Yao and C. A. Randalld, *J. Mater. Chem.*, 2011, **21**,

View Article Online
DOI: 10.1039/C6RA20197K

18412.

25. F. Shi and H. L. Dong, *Cryst. Eng. Comm.*, 2012, **14**, 3373.
26. Z. F. Fu, P. Liu, J. L. Ma, X. G. Zhao and H. W. Zhang, *J. Eur. Ceram. Soc.*, 2010, **30**, 341.
27. J. Varghese, T. Joseph, K. P. Surendran, T. P. D. Rajan and M. T. Sebastian, *Dalton Trans.*, 2015, **44**, 5146.
28. H. L. Dong and F. Shi, *Cryst. Eng. Comm.*, 2012, **14**, 8268.
29. A. F. Kapustinskii, *Rev. Chem. Soc.*, 1956, **10**, 283.
30. D. F. Xue and S. Y. Zhang, *J. Phys. : Condens. Matter.*, 1996, **8**, 1949.
31. Z. J. Wu, Q. B. Meng and S. Y. Zhang, *Phys. Rev. B*, 1998, **58**, 958.
32. Q. B. Meng, Z. J. Wu and S. Y. Zhang, *Phys. Cond. Mat.*, 1998, **10**, 85.
33. Z. J. Wu and S. Y. Zhang, *Int. J. Quantum Chem.*, 1999, **73**, 433.
34. P. Zhang, Y. G. Zhao and Y. X. Wang, *Dalton Trans.*, 2015, **44**, 10932.
35. R. T. Sanderson, *Inorg. Nucl. Chem.*, 1968, **30**, 375.
36. R. T. Sanderson, *J. Am. Chem. Soc.*, 1983, **105**, 2259.
37. Y. R. Luo, Comprehensive Handbook of Chemical Bond Energies, CRC Press, Boca Raton, 2007.
38. Y. G. Zhao and P. Zhang, *RSC Adv.*, 2015, **5**, 97746.
39. H. T. Wu and E. S. Kim, *RSC Adv.*, 2016, **6**, 47443.
40. R. D. Shannon and G. R. Rossman, *Am. Mineral.*, 1992, **77**, 94.
41. R. D. Shannon, *J. Appl. Phys.*, 1993, **73**, 348.
42. F. Shi and H. L. Dong, *Dalton Trans.*, 2011, **40**, 6659.
43. F. Shi and H. L. Dong, *Dalton Trans.*, 2011, **40**, 11591.
44. P. Zhang, Y. G. Zhao and L. X. Li, *Phys. Chem. Chem. Phys.*, 2015, **17**, 16692.
45. A. J. Bosman and E. E. Havinga, *Phys. Rev.*, 1963, **129**, 1593.
46. E. S. Kim and C. J. Jeon, *J. Eur. Ceram. Soc.*, 2010, **30**, 341.

View Article Online
DOI: 10.1039/C6RA20197K

Figures captions

Fig. 1 The XRD patterns of the $Zn_{1-x}Co_xZrNb_2O_8$ (x = 0, 0.02, 0.04, 0.06, 0.08, 0.10) ceramics sintered at 1150 °C for 4 h.

Fig. 2 Rietveld refinement of the $Zn_{1-x}Co_xZrNb_2O_8$ ceramics((a) x=0, (b) x=0.02, (c) x=0.04, (d) x=0.06, (e) x=0.08, (f) x=0.10).

Fig. 3 Schematic representation of the $Zn_{1-x}Co_xZrNb_2O_8$ (2×2×2) supercell and the A-site (A = Zn^{2+}/Co^{2+}, Zr^{4+}) and B-site (B = Nb^{5+}) oxygen octahedrons of the $Zn_{0.94}Co_{0.06}ZrNb_2O_8$ with the bond lengths.

Fig. 4 (a) Raman spectra of $Zn_{1-x}Co_xZrNb_2O_8$ ceramics. (b) Deconvoluted Raman spectra of the $Zn_{0.94}Co_{0.06}ZrNb_2O_8$ ceramics.

Fig. 5 (a) Apparent densities of $Zn_{1-x}Co_xZrNb_2O_8$ (x = 0, 0.02, 0.04, 0.06, 0.08, 0.10) ceramics as a function of sintering temperature. (b) Relative densities of $Zn_{1-x}Co_xZrNb_2O_8$ (x = 0, 0.02, 0.04, 0.06, 0.08, 0.10) ceramics sintered at 1150 °C.

Fig. 6 SEM micrographs of $Zn_{1-x}Co_xZrNb_2O_8$ ceramics sintered at 1150 °C for 4 h (a-f corresponding to x = 0, x = 0.02, x = 0.04, x = 0.06, x = 0.08, x = 0.10).

Fig. 7 The coordination number and the charge distribution of ions in the $Zn_{1-x}Co_xZrNb_2O_8$ (x = 0, 0.02, 0.04, 0.06, 0.08, 0.10) ceramics.

Fig. 8 The bond ionicity, lattice energy, bond energy and coefficient of thermal expansion as a variation of A-O bonds for $Zn_{1-x}Co_xZrNb_2O_8$ (x = 0, 0.02, 0.04, 0.06, 0.08, 0.10) ceramics.

Fig. 9 (a) The dielectric constants of $Zn_{1-x}Co_xZrNb_2O_8$ (x = 0, 0.02, 0.04, 0.06, 0.08, 0.10) ceramics as a function of the sintering temperatures. (b) The dielectric constants (ε_r), observed dielectric polarizability ($\alpha_{obs.}$) and theoretical dielectric polarizability ($\alpha_{theo.}$) of $Zn_{1-x}Co_xZrNb_2O_8$ (x = 0, 0.02, 0.04, 0.06, 0.08, 0.10) ceramics sintered at 1150 °C. (c) The variation of the bond ionicity of Nb-O bonds and Raman shift of $Zn_{1-x}Co_xZrNb_2O_8$ (x = 0, 0.02, 0.04, 0.06, 0.08, 0.10) ceramics sintered at 1150 °C.

Fig. 10 (a) The $Q \cdot f$ values of $Zn_{1-x}Co_xZrNb_2O_8$ (x = 0, 0.02, 0.04, 0.06, 0.08, 0.10) ceramics as a function of the sintering temperatures. (b) The relationships among the $Q \cdot f$ values, lattice energy of Nb-O bonds and FWHM of peaks of $Zn_{1-x}Co_xZrNb_2O_8$ (x = 0, 0.02, 0.04, 0.06, 0.08, 0.10) ceramics sintered at 1150 °C.

Fig. 11 The variations of the temperature coefficient of resonant frequency (τ_f), thermal expansion

View Article Online
DOI: 10.1039/C6RA20197K

coefficient of the Nb-O bonds (α_{Nb-O}), bond valence of the Nb-O bonds (V_{Nb-O}), Nb-site octahedral distortion (δ_{Nb-O}) and bond energy of Nb-O bonds (E_{Nb-O}) for $Zn_{1-x}Co_xZrNb_2O_8$ (x = 0, 0.02, 0.04, 0.06, 0.08, 0.10) ceramics sintered at 1150 °C.

Table captions

Table 1 Atomic positions and occupancies of $Zn_{0.94}Co_{0.06}ZrNb_2O_8$ ceramics.

Table 2 The refinement parameters of $Zn_{1-x}Co_xZrNb_2O_8$ (x = 0, 0.02, 0.04, 0.06, 0.08, 0.10) ceramics sintered at 1150 °C.

Table 3 The bond lengths of the Zn/Co-O, Zr-O and Nb-O bonds in $Zn_{1-x}Co_xZrNb_2O_8$ (x = 0, 0.02, 0.04, 0.06, 0.08, 0.10) ceramics

Table 4 Relative densities, octahedral distortion and the bond valence of $Zn_{1-x}Co_xZrNb_2O_8$ (x = 0, 0.02, 0.04, 0.06, 0.08, 0.10) ceramics.

Table 5 Peak positions of typical vibration modes in Raman spectra.

Table 6 Full width at half maximum (FWHM) of typical vibration modes in Raman spectra.

Table 7 Bond ionicity of $Zn_{1-x}Co_xZrNb_2O_8$ (x = 0, 0.02, 0.04, 0.06, 0.08, 0.10) ceramics sintered at 1150 °C.

Table 8 Lattice energy of $Zn_{1-x}Co_xZrNb_2O_8$ (x = 0, 0.02, 0.04, 0.06, 0.08, 0.10) ceramics sintered at 1150 °C.

Table 9 Bond energy of $Zn_{1-x}Co_xZrNb_2O_8$ (x = 0, 0.02, 0.04, 0.06, 0.08, 0.10) ceramics sintered at 1150 °C.

Table 10 Thermal expansion coefficient of $Zn_{1-x}Co_xZrNb_2O_8$ (x = 0, 0.02, 0.04, 0.06, 0.08, 0.10) ceramics sintered at 1150 °C.

View Article Online
DOI: 10.1039/C6RA20197K

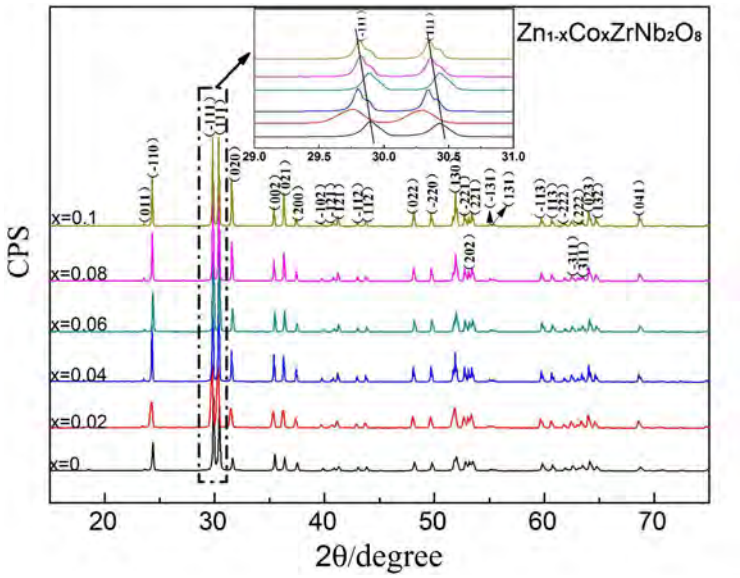

Fig. 1

View Article Online
DOI: 10.1039/C6RA20197K

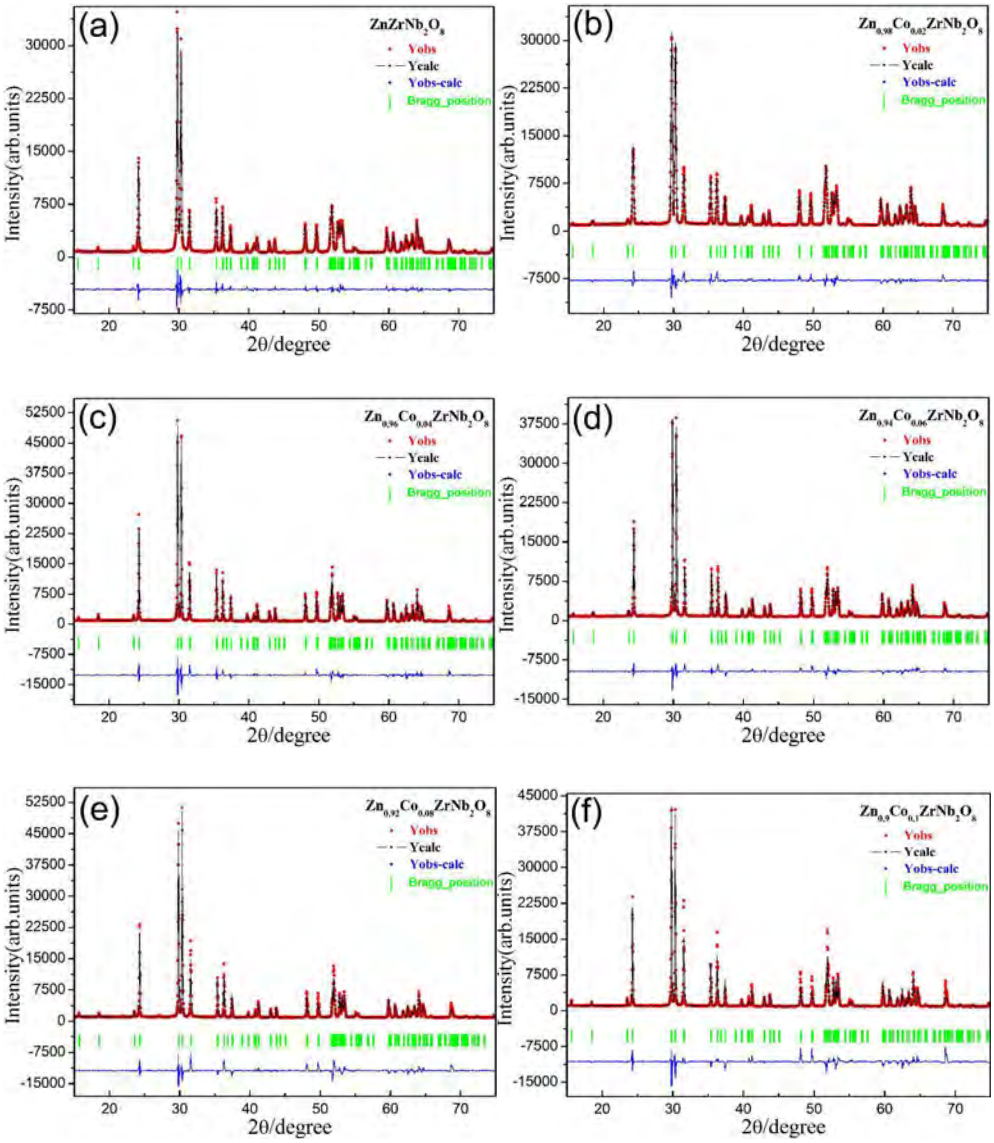

Fig. 2

View Article Online
DOI: 10.1039/C6RA20197K

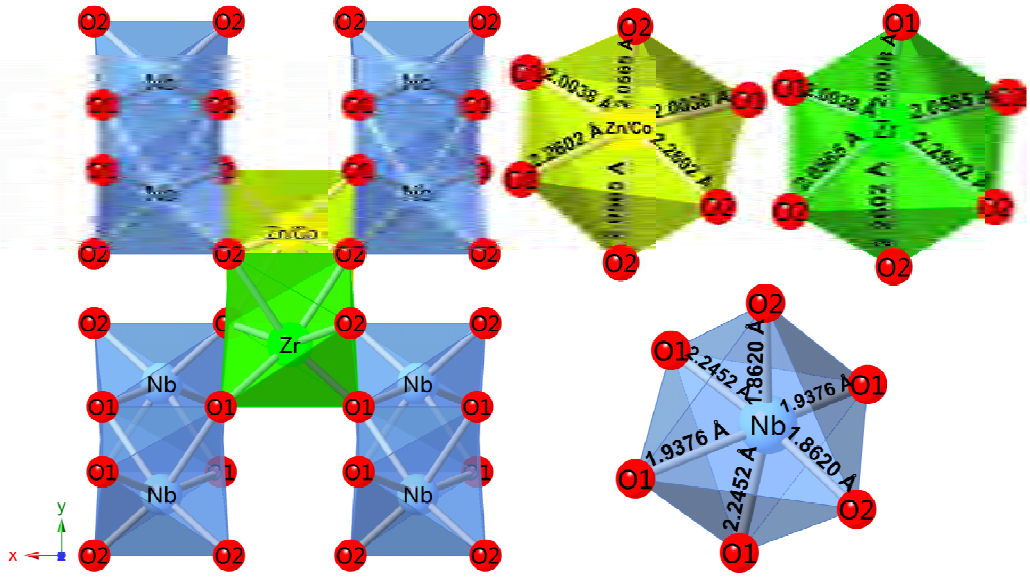

Fig. 3

View Article Online
DOI: 10.1039/C6RA20197K

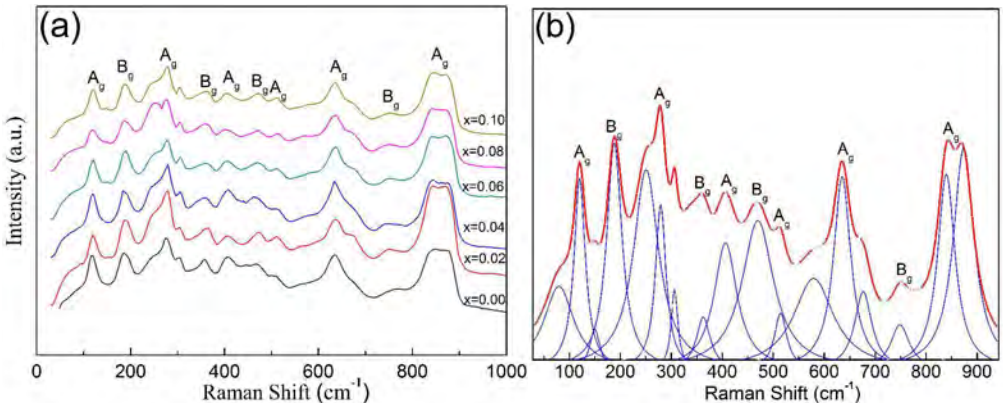

Fig. 4

View Article Online
DOI: 10.1039/C6RA20197K

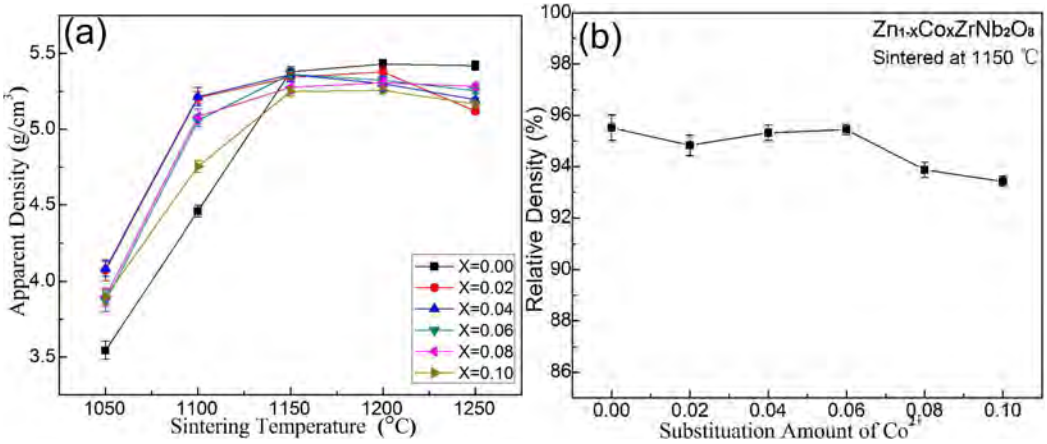

Fig. 5

View Article Online
DOI: 10.1039/C6RA20197K

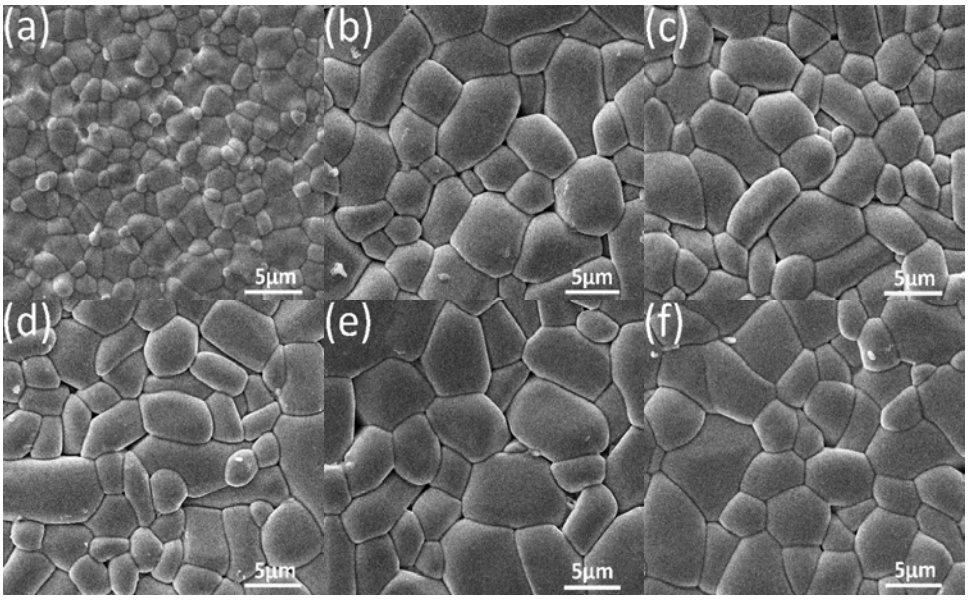

Fig. 6

View Article Online
DOI: 10.1039/C6RA20197K

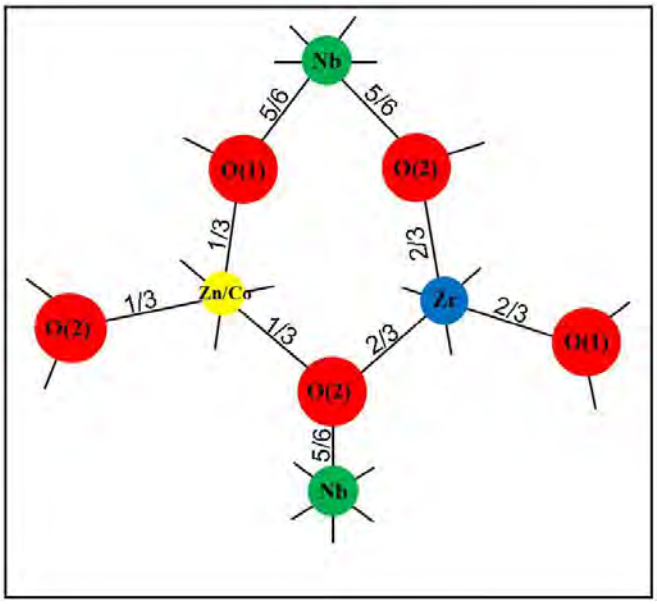

Fig. 7

View Article Online
DOI: 10.1039/C6RA20197K

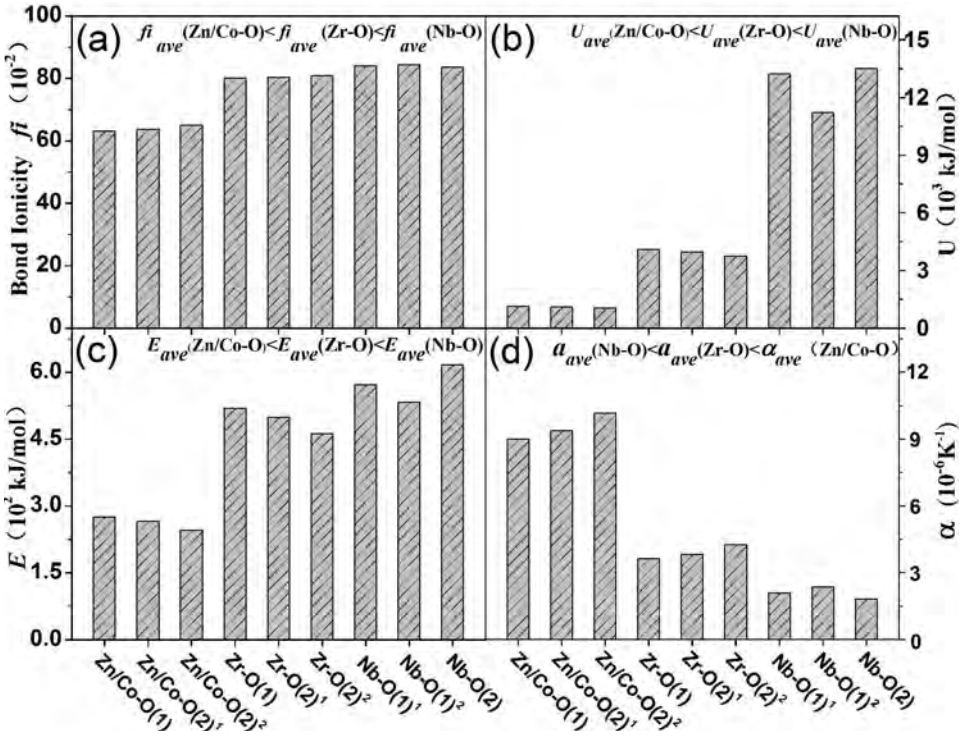

Fig. 8

View Article Online
DOI: 10.1039/C6RA20197K

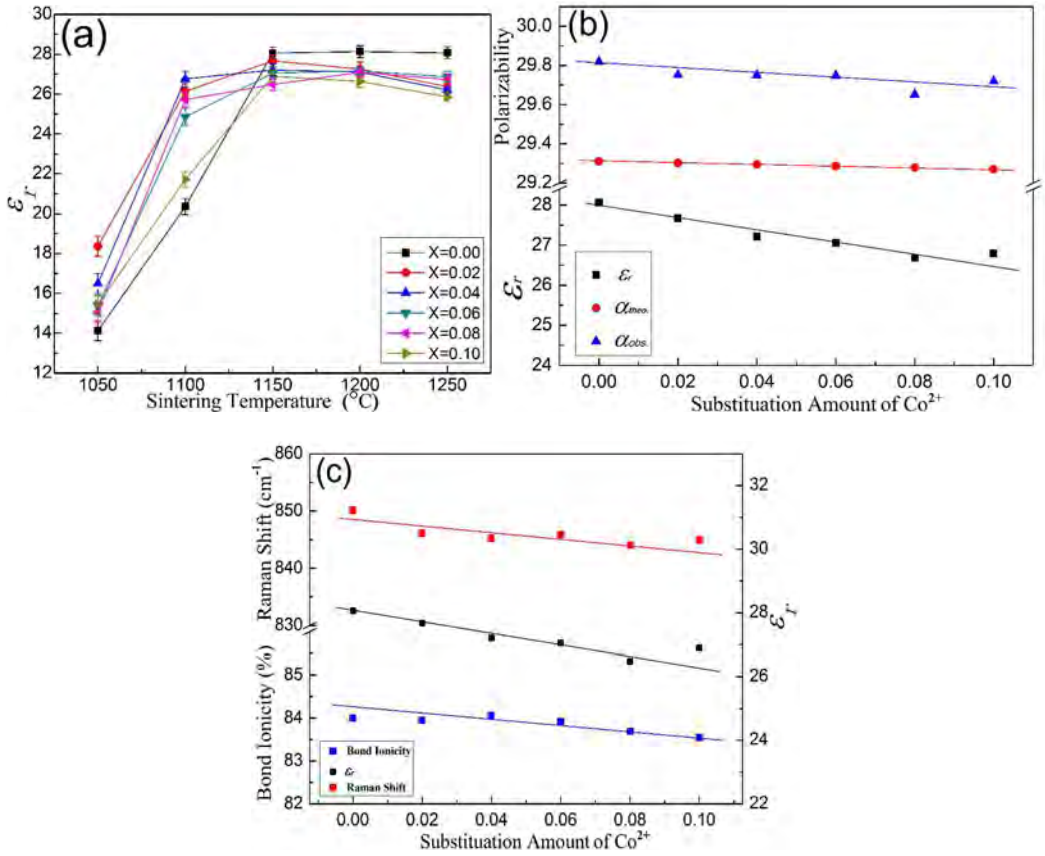

Fig. 9

View Article Online
DOI: 10.1039/C6RA20197K

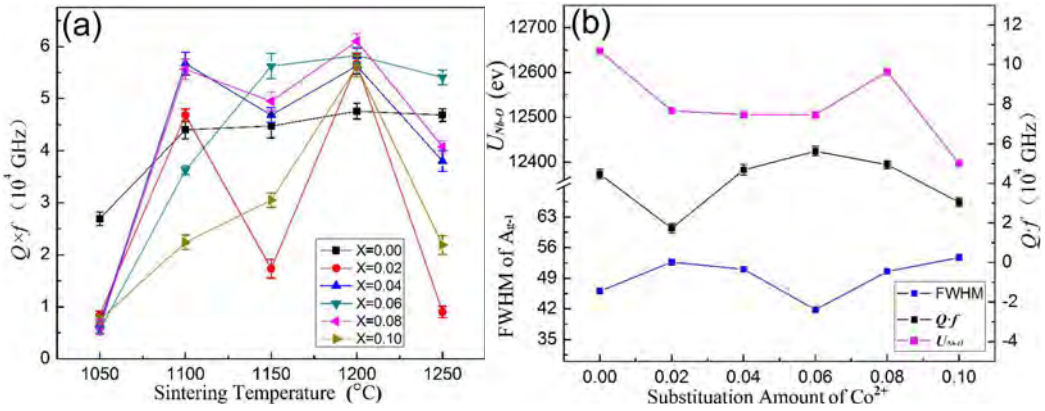

Fig. 10

View Article Online
DOI: 10.1039/C6RA20197K

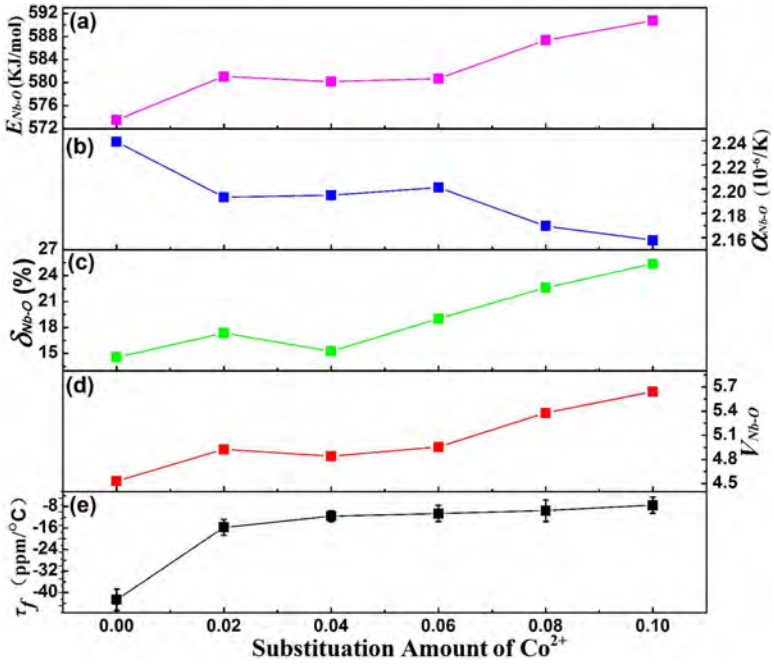

Fig. 11

View Article Online
DOI: 10.1039/C6RA20197K

Table 1

Atom	Wyckoff position	x	y	z	Occ.
Zn/Co	2f	0.500(0)	0.687(8)	0.250(0)	0.500(0)
Zr	2f	0.500(0)	0.687(8)	0.250(0)	0.500(0)
Nb	2e	0.000(0)	0.181(2)	0.250(0)	1.000(0)
O1	4g	0.267(1)	0.374(1)	0.414(3)	2.000(0)
O2	4g	0.214(7)	0.123(2)	0.935(7)	2.000(0)

View Article Online
DOI: 10.1039/C6RA20197K

Table 2

$Zn_{1-x}Co_xZrNb_2O_8$	x=0.00	x=0.02	x=0.04	x=0.06	x=0.08	x=0.10
a (Å)	4.811(9)	4.809(2)	4.812(5)	4.814(5)	4.812(3)	4.813(4)
b (Å)	5.678(4)	5.678(3)	5.682(1)	5.681(1)	5.678(9)	5.680(3)
c (Å)	5.079(6)	5.078(6)	5.080(0)	5.082(0)	5.081(7)	5.082(1)
β (Å)	91.370(0)	91.402(0)	91.403(0)	91.414(0)	91.402(7)	91.405(0)
V (Å^3)	138.753(4)	138.645(8)	138.881(6)	138.958(7)	138.831(7)	138.912(5)
R_P (%)	5.290(0)	5.070(0)	6.660(0)	6.470(0)	8.380(0)	10.600(0)
R_{WP} (%)	7.210(0)	6.630(0)	8.790(0)	8.760(0)	11.300(0)	14.700(0)
$\chi 2$	2.700(0)	2.360(0)	2.560(0)	2.500(0)	2.470(0)	2.460(0)

View Article Online
DOI: 10.1039/C6RA20197K

Table 3

Bond Type	x=0.00	x=0.02	x=0.04	x=0.06	x=0.08	x=0.10
Zn/Co-O(1)	1.985(3)	1.996(6)	2.016(1)	2.003(8)	1.997(5)	2.006(1)
Zn/Co-O(2)[1]	2.064(9)	2.046(9)	2.037(9)	2.056(5)	2.048(1)	2.002(7)
Zn/Co-O(2)[2]	2.233(2)	2.273(9)	2.244(7)	2.260(2)	2.274(6)	2.390(6)
Zr-O(1)	1.985(3)	1.996(6)	2.016(1)	2.003(8)	1.997(5)	2.006(1)
Zr-O(2)[1]	2.064(9)	2.046(9)	2.037(9)	2.056(5)	2.048(1)	2.002(7)
Zr-O(2)[2]	2.233(2)	2.273(9)	2.244(7)	2.260(2)	2.274(6)	2.390(6)
Nb-O(1)[1]	2.033(3)	1.951(1)	1.948(1)	1.937(6)	1.867(6)	1.858(9)
Nb-O(1)[2]	2.182(9)	2.215(9)	2.197(7)	2.245(2)	1.952(2)	2.311(1)
Nb-O(2)	1.886(6)	1.866(7)	1.890(9)	1.862(0)	2.216(6)	1.805(4)

View Article Online
DOI: 10.1039/C6RA20197K

Table 4

$Zn_{1-x}Co_xZrNb_2O_8$	Bond type	d_{ave} (Å)	R_{ij} (Å)	δ (%)	V_{ij}	R.D. (%)
X=0	Zn/Co-O	2.094(5)	1.704(0)	11.835(9)	2.167(6)	95.523(2)
	Zr-O	2.094(5)	1.928(0)	11.835(9)	3.973(6)	
	Nb-O	2.034(2)	1.911(0)	14.565(4)	4.532(5)	
X=0.02	Zn/Co-O	2.105(8)	1.704(0)	13.168(4)	2.125(9)	94.828(9)
	Zr-O	2.105(8)	1.928(0)	13.168(4)	3.897(1)	
	Nb-O	2.011(2)	1.911(0)	17.362(5)	4.926(3)	
X=0.04	Zn/Co-O	2.099(6)	1.704(0)	10.887(9)	2.132(6)	95.322(0)
	Zr-O	2.099(6)	1.928(0)	10.887(9)	3.912(0)	
	Nb-O	2.012(2)	1.911(0)	15.246(7)	4.842(4)	
X=0.06	Zn/Co-O	2.106(8)	1.703(0)	12.169(9)	2.101(6)	95.442(9)
	Zr-O	2.106(8)	1.928(0)	12.169(9)	3.857(6)	
	Nb-O	2.014(9)	1.911(0)	19.018(0)	4.954(9)	
X=0.08	Zn/Co-O	2.106(7)	1.703(0)	13.153(2)	2.114(2)	93.865(7)
	Zr-O	2.106(7)	1.928(0)	13.153(2)	3.858(5)	
	Nb-O	2.012(1)	1.911(0)	22.604(6)	5.277(9)	
X=0.10	Zn/Co-O	2.133(1)	1.703(0)	18.184(5)	2.082(0)	93.424(2)
	Zr-O	2.133(1)	1.928(0)	18.184(5)	3.826(6)	
	Nb-O	1.991(8)	1.911(0)	25.389(1)	5.641(3)	

View Article Online
DOI: 10.1039/C6RA20197K

Table 5

Vibrational mode	x=0(cm^{-1})	x=0.02 (cm^{-1})	x=0.04 (cm^{-1})	x=0.06 (cm^{-1})	x=0.08 (cm^{-1})	x=0.10 (cm^{-1})
A_g	118.228(6)	118.370(2)	119.523(4)	120.170(4)	119.360(6)	120.100(6)
B_g	186.432(6)	186.624(9)	187.396(9)	188.195(3)	187.891(6)	188.256(2)
A_g	278.258(7)	277.518(5)	278.297(7)	279.156(0)	278.227(5)	277.935(7)
B_g	358.398(6)	358.127(0)	353.673(7)	362.771(9)	360.339(3)	363.555(5)
A_g	405.883(1)	409.289(5)	406.931(5)	406.431(2)	405.677(4)	406.290(8)
B_g	471.817(9)	469.913(2)	466.972(6)	469.757(0)	467.640(1)	468.248(7)
A_g	509.917(5)	510.166(6)	513.402(9)	514.374(8)	513.386(1)	513.073(2)
A_g	634.800(1)	634.793(0)	634.985(5)	635.234(9)	634.632(7)	634.898(1)
B_g	760.431(9)	760.511(5)	753.415(4)	748.673(6)	751.191(2)	751.880(8)
A_{g-1}	843.818(1)	841.432(5)	842.158(8)	839.538(3)	840.857(9)	839.426(5)
A_{g-2}	876.838(3)	874.389(2)	874.975(3)	873.717(2)	874.541(4)	872.084(1)

View Article Online
DOI: 10.1039/C6RA20197K

Table 6

Vibrational mode	x=0	x=0.02	x=0.04	x=0.06	x=0.08	x=0.10
A_g	29.827(4)	29.055(7)	27.310(1)	27.211(2)	30.192(1)	26.397(6)
B_g	44.735(3)	44.685(6)	41.012(3)	36.410(9)	36.986(2)	34.183(9)
A_g	31.026(0)	32.683(1)	27.741(3)	25.482(5)	25.1637(9)	23.851(5)
B_g	37.815(9)	38.012(7)	75.812(2)	33.177(2)	46.932(5)	23.942(7)
A_g	50.27(9)	59.965(0)	40.311(5)	55.030(2)	59.326(3)	45.116(8)
B_g	53.278(1)	58.937(9)	71.574(5)	75.703(3)	67.445(8)	69.143(9)
A_g	40.229(9)	38.374(6)	36.135(8)	29.364(4)	29.519(0)	28.779(2)
A_g	51.416(6)	49.526(9)	51.142(0)	41.341(5)	49.203(1)	39.968(6)
B_g	69.423(6)	70.505(5)	79.574(4)	44.495(2)	74.127(9)	62.682(3)
A_{g-1}	46.102(8)	52.705(1)	51.048(4)	41.827(5)	50.573(6)	53.753(9)
A_{g-2}	49.333(6)	51.001(8)	33.456(8)	34.803(1)	41.983(9)	42.148(4)

View Article Online
DOI: 10.1039/C6RA20197K

Table 7

$Zn_{1-x}Co_xZrNb_2O_8$	Bond ionicity f_i (%)					
	x=0	x=0.02	x=0.04	x=0.06	x=0.08	x=0.10
Zn(Co)-O(1)×2	63.027(2)	63.176(9)	63.499(8)	63.207(4)	63.186(0)	62.882(2)
Zn(Co)-O(2)[1]×2	63.732(0)	63.624(5)	63.692(9)	63.671(0)	63.635(5)	62.851(5)
Zn(Co)-O(2)[2]×2	65.002(7)	65.317(2)	65.277(1)	65.192(0)	65.322(4)	65.607(4)
Zr-O(1)×2	80.045(9)	80.128(2)	80.319(9)	80.130(8)	80.132(5)	79.873(5)
Zr-O(2)[1]×2	80.360(9)	80.328(5)	80.406(1)	80.337(4)	80.333(6)	79.859(7)
Zr-O(2)[2]×2	80.888(7)	81.027(5)	81.068(9)	80.965(8)	81.029(7)	80.970(0)
Nb-O(1)[1]×2	84.040(9)	83.830(4)	83.918(3)	83.763(0)	83.440(3)	83.252(1)
Nb-O(1)[2]×2	84.381(1)	84.472(4)	84.540(1)	84.497(1)	83.734(4)	84.350(7)
Nb-O(2)×2	83.580(1)	83.536(4)	83.722(8)	83.495(0)	84.374(1)	83.036(0)
$Af_{iZn/Co-O}$	63.920(6)	64.039(5)	64.156(6)	64.023(5)	64.047(7)	63.780(4)
Af_{iZr-O}	80.431(8)	80.494(7)	80.598(3)	80.478(0)	80.498(6)	80.234(4)
Af_{iNb-O}	84.000(1)	83.946(4)	84.060(4)	83.918(4)	83.649(6)	83.546(3)

Notes: Af_i was the average of the bond ionicity; (1)and (2) were used to distinguish oxygen atoms with different coordinate positions and the [1] and [2] were used to distinguish the oxygen atoms with different bond lengths.

View Article Online
DOI: 10.1039/C6RA20197K

Table 8

$Zn_{1-x}Co_xZrNb_2O_8$	Lattice energy U (eV)					
	x=0	x=0.02	x=0.04	x=0.06	x=0.08	x=0.10
Zn(Co)-O(1)×2	1126.(0)	1121.(0)	1112.(0)	1118.(0)	1121.(0)	1117.(0)
$Zn(Co)-O(2)^1$×2	1091.(0)	1099.(0)	1102.(0)	1095.(0)	1098.(0)	1119.(0)
$Zn(Co)-O(2)^2$×2	1025.(0)	1010.(0)	1020.(0)	1015.(0)	1009.(0)	970.(0)
Zr-O(1)×2	4082.(0)	4065.(0)	4036.(0)	4054.(0)	4064.(0)	4051.(0)
$Zr-O(2)^1$×2	3963.(0)	3990.(0)	4003.(0)	3976.(0)	3988.(0)	4055.(0)
$Zr-O(2)^2$×2	3732.(0)	3681.(0)	3717.(0)	3697.(0)	3679.(0)	3538.(0)
$Nb-O(1)^1$×2	13223.(0)	12766.(0)	12781.(0)	13091.(0)	13280.(0)	12379.(0)
$Nb-O(1)^2$×2	11219.(0)	11595.(0)	11669.(0)	11336.(0)	12860.(0)	11729.(0)
Nb-O(2)×2	13503.(0)	13185.(0)	13063.(0)	13379.(0)	11692.(0)	13084.(0)
$AU_{Zn/Co-O}$	1081.(7)	1077.(7)	1078.(0)	1076.(0)	1076.(0)	1068.(7)
AU_{Zr-O}	3926.(7)	3912.(0)	3919.(7)	3909.(0)	3910.(3)	3881.(3)
AU_{Nb-O}	12648.(3)	12515.(3)	12504.(3)	12602.(0)	12610.(7)	12397.(0)

Notes: AU was the average of the lattice energy; (1)and (2) were used to distinguish oxygen atoms with different coordinate positions and the ^{1} and ^{2} were used to distinguish the oxygen atoms with different bond lengths.

View Article Online
DOI: 10.1039/C6RA20197K

Table 9

$Zn_{1-x}Co_xZrNb_2O_8$	Bond energy E (kJ mol^{-1})					
	x=0	x=0.02	x=0.04	x=0.06	x=0.08	x=0.10
Zn(Co)-O(1)×2	275.927(1)	276.941(8)	276.687(2)	280.711(1)	283.828(2)	284.743(2)
Zn(Co)-O(2)[1]×2	265.290(4)	270.136(4)	273.727(4)	273.517(6)	276.816(0)	285.226(6)
Zn(Co)-O(2)[2]×2	245.297(4)	243.169(0)	248.509(4)	248.866(9)	249.251(3)	238.945(6)
Zr-O(1)×2	519.124(2)	516.186(1)	511.193(5)	514.331(4)	515.953(6)	513.741(7)
Zr-O(2)[1]×2	499.112(4)	503.501(5)	505.725(1)	501.151(1)	503.206(5)	514.613(9)
Zr-O(2)[2]×2	461.498(0)	453.237(7)	459.133(6)	455.985(0)	453.098(2)	431.112(4)
Nb-O(1)[1]×2	571.740(8)	595.828(3)	596.745(9)	599.979(7)	628.467(7)	625.380(5)
Nb-O(1)[2]×2	532.557(9)	524.626(9)	528.971(5)	517.780(4)	601.492(6)	503.016(2)
Nb-O(2)×2	616.198(8)	622.767(8)	614.797(3)	624.339(8)	530.461(2)	643.913(1)
$AE_{Zn/Co-O}$	262.171(6)	263.415(7)	266.308(0)	267.698(6)	269.965(2)	269.638(5)
AE_{Zr-O}	493.244(9)	490.975(1)	492.017(4)	490.489(2)	490.752(8)	486.489(3)
AE_{Nb-O}	573.499(2)	581.074(3)	580.171(6)	580.699(6)	586.807(2)	590.770(1)

Notes: AE was the average of the bond energy; (1)and (2) were used to distinguish oxygen atoms with different coordinate positions and the [1] and [2] were used to distinguish the oxygen atoms with different bond lengths.

View Article Online
DOI: 10.1039/C6RA20197K

Table 10

$Zn_{1-x}Co_xZrNb_2O_8$	Thermal expansion coefficient (10^{-6}/K)					
	x=0	x=0.02	x=0.04	x=0.06	x=0.08	x=0.10
Zn(Co)-O(1)×2	9.617(3)	9.674(3)	9.778(3)	9.708(8)	9.674(3)	9.720(3)
Zn(Co)-O(2)^1×2	10.027(4)	9.931(4)	9.895(7)	9.979(3)	9.943(3)	9.697(3)
Zn(Co)-O(2)^2×2	10.877(1)	11.085(7)	10.946(0)	11.015(5)	11.099(9)	11.673(6)
Zr-O(1)×2	3.885(3)	3.914(8)	3.965(7)	3.934(0)	3.916(5)	3.939(3)
Zr-O(2)^1×2	4.097(1)	4.047(9)	4.024(5)	4.073(3)	4.051(6)	3.932(3)
Zr-O(2)^2×2	4.546(8)	4.653(7)	4.579(5)	4.619(9)	4.658(0)	4.969(9)
Nb-O(1)^1×2	2.236(5)	2.072(6)	2.066(5)	2.046(1)	1.878(0)	1.891(5)
Nb-O(1)^2×2	2.5360(0)	2.601(9)	2.565(3)	2.661(3)	2.045(1)	2.795(3)
Nb-O(2)×2	1.945(2)	1.906(7)	1.953(5)	1.896(8)	2.573(4)	1.786(6)
$A\alpha_{Zn/Co-O}$	10.174(0)	10.230(5)	10.206(7)	10.234(5)	10.239(2)	10.363(7)
$A\alpha_{Zr-O}$	4.176(4)	4.205(5)	4.189(4)	4.209(1)	4.208(7)	4.280(5)
$A\alpha_{Nb-O}$	2.239(2)	2.193(5)	2.195(1)	2.201(4)	2.165(5)	2.157(8)

Notes: Aα was the average of the thermal expansion coefficient; (1)and (2) were used to distinguish oxygen atoms with different coordinate positions and the ^{1} and ^{2} were used to distinguish the oxygen atoms with different bond lengths.